PROCEEDINGS, 41st Workshop on Geothermal Reservoir Engineering
Stanford University, Stanford, California, February 22-24, 2016
SGP-TR-209

Thermal Forecasting Ability of Temperature-Sensitive Tracers

Morgan Ames, Philip Brodrick and Roland Horne

Energy Resources Engineering, 367 Panama Street, Green Earth Sciences 065, Stanford University, Stanford, CA 94305-2220

mames@stanford.edu

Keywords: tracers, thermal breakthrough, particle tracers, reactive tracers, discrete fracture networks

ABSTRACT

The development of a reliable and accurate method to predict thermal breakthrough time is a significant open problem in geothermal reservoir engineering. Such a method would enable more informed decisions to be made regarding reservoir management. Methods developed at present include analytical models and solute tracers, both of which have limitations. The use of particles as temperature-sensitive tracers is a promising approach due to the high degree of control of the physical and chemical properties of nanomaterials and micromaterials. This could potentially be exploited to infer temperature and measurement location, which could in turn provide useful information about thermal breakthrough.

In order to assess whether particle tracers can provide more useful information about future thermal behavior of reservoirs than existing solute tracers, models were developed for both solute tracers and particle tracers. Three existing solute tracer types were modeled: conservative solute tracers (CSTs), reactive solute tracers with temperature dependent reaction kinetics (RSTs), and sorbing solute tracers that sorb reversibly to fracture walls (SSTs). Additionally three particle tracers which have not yet been developed in practice were modeled: dye releasing tracers (DRTs) that release a solute dye at a specified temperature threshold is reached, threshold nanoreactor tracers (TNRTs) with an encapsulated reaction that does not begin until a specified temperature threshold is reached, and temperature-time tracers (TTTs) capable of recording detailed temperature-time histories of each particle. In this study, TTTs represent the most informative tracer with respect to thermal breakthrough. These models were used in the context of an inverse problem in which synthetic tracer data was calculated for several "true" discrete fracture networks. Computational optimization was used to match the location, length, and orientation of a variable number of fractures. Finally, the thermal behavior of the fracture networks with the best fit to the data was compared to that of the true fracture networks, and the forecast accuracy was compared for all tracer types.

1. INTRODUCTION

One of the most significant open problems in geothermal reservoir engineering is the development of a reliable and accurate method to predict thermal breakthrough. Reinjection of cooled geothermal fluid is practiced in many of the world's geothermal fields in order to maintain pressure, prevent geothermal fluid from entering aquifers and rivers by reinjecting it, and to sweep as much thermal energy from the reservoir as possible (Horne 2010). Reinjected fluid cools the reservoir at the fluid-rock interface near the injection well, meaning that subsequent reinjected fluid must travel farther from the injection well before it is heated to the original reservoir temperature. This cooling that propagates from the injection well to the production well is called the thermal front. Thermal breakthrough is said to occur when the thermal front reaches the production well, and it spells the end of the useful life of the production well. The ability to accurately predict thermal breakthrough far in advance would enable more informed decisions to be made about reservoir management.

Much effort has been and continues to be devoted to thermal breakthrough prediction, but no fully reliable method has been developed at present. Methods have been developed that make use of thermal modeling to calculate thermal breakthrough time, but are very difficult to apply due to the uncertain flowpath geometry. Tracer tests using conservative solutes can be useful in reservoir characterization, but their utility is typically limited to evaluating well connectivity and estimating reservoir size. Others have proposed the use of reactive solute tracers with temperature dependent reaction kinetics to estimate reservoir temperature. With several field demonstrations to date, this method shows promise, but it provides limited information about the thermal front and requires multiple tracer tests at different times (Tester et al. 1986, Rose and Adams 1994, and Plummer et al. 2012). Because reservoir flow conditions can change in between tracer tests due to natural or operational changes, it can be difficult to reproduce tracer tests due to changing flowpaths, which may render multiple reactive tracer tests to estimate thermal front evolution infeasible. Researchers including Reimus et al. 2012, Williams et al. 2013, Dean et al. 2012, Dean et al. 2015, Leecaster et al. 2012, and Hawkins et al. 2015 have also proposed the use of sorbing solute tracers to estimate reservoir heat transfer surface area, as sorption surface area and heat transfer surface area are closely related. This would be a very useful parameter to know, but other factors can also influence reservoir temperature distribution. Fracture network geometry and the resulting spacing between fractures influences the temperature as well, because thermal interference can occur when the region of rock between two closely spaced fractures is depleted of its heat.

With the exception of solute tracers, current technology only allows temperature measurement at the well-bore. The focus of this research was a variation of the reactive tracer concept, in which nanoparticles would be used as flow-through sensors that undergo detectable and irreversible changes at a particular threshold temperature. Nanoparticles have excellent potential as temperature measurement tools because they can be synthesized with a great degree of control over their structure and their physical and chemical properties, making possible a host of different sensing mechanisms. Furthermore, their small size enables them to fit through pore spaces. Finally, nanoparticles often exhibit different transport behavior than solutes because they experience less diffusion and tend to

stay in high-velocity streamlines (Reimus 1995, Becker et al. 1999). These differences in transport behavior could help estimate the location of temperature measurements, allowing one to map the thermal front in a geothermal reservoir. Because the shape of the thermal front contains information about the geometry of the fracture network, a single tracer test could potentially provide a great deal of information about thermal breakthrough.

While nanoparticle tracers show great promise, they also have their own unique technical challenges. The ideal particle tracer has high mobility (i.e. experiences minimal deposition and aggregation) in the reservoir, undergoes an irreversible temperature sensing mechanism at the temperature of interest, is readily detectable and collectible at the production well in low concentrations, provides information about the location of the temperature measurement, and is environmentally benign. The first and perhaps the most significant of challenges associated with these criteria is synthesizing nanoparticles that can be transported through the subsurface without significant particle aggregation or deposition occurring. It is desirable to prevent particle aggregation because the formation of larger particle clusters can enhance particle deposition due to gravitational settling or size exclusion. This is made difficult by the fact that geothermal fluids often have high ionic strength and high temperature, conditions which are very favorable for particle aggregation.

Because the development of temperature-sensitive particle tracers presents many significant technical challenges, it is useful to determine in advance whether they provide more useful information about thermal breakthrough than existing solute tracers. To this end, models were developed of both solute and particle tracers, and synthetic tracer data was generated using these models for several "true" fracture networks. These synthetic data were then matched using an optimization program called PSO-MADS, which was developed by Isebor (2013). The decision variables used in optimizations were the existence, locations, lengths, and orientations of fractures within the network. The thermal behavior of the fracture networks corresponding to the best fit for each tracer type was then calculated and compared to the thermal behavior of the true fracture networks. Finally, the tracers were ranked in order of their forecast accuracy for each true fracture network.

2. METHODS

The particle tracers that were modeled include two types proposed recently by geothermal researchers: Dye-Releasing Tracers (DRTs), or particles that release a solute dye upon encountering a threshold temperature of interest, and Threshold Nano-Reactor Tracers (TNRTs), or nanoparticles encapsulating one or more reactants that are prevented from reacting until encountering a threshold temperature of interest. Williams et al. (2010) proposed a dye-release mechanism for measuring geothermal temperatures, in which particle tracers release encapsulated dyes once a threshold temperature is reached. In an attempt to synthesize dye-releasing particle tracers for geothermal applications, Alaskar et al. (2015) synthesized silica nanoparticles with the fluorescent dye Oregon 488 covalently attached to their surfaces using temperature sensitive amino groups as the links between particle surfaces and dye molecules. The fluorescence spectrum of these particles was measured and found to be distinct from that of the free dye. These particles were also subjected to a heating experiment, and changes in the fluorescence spectrum were observed after heating. Redden et al. (2010) proposed the use of contained nanoreactors that make use of thermoluminscence or polymer racemization to infer the thermal history of a geothermal reservoir. They synthesized mineral particles and coated them with various polymers, but reported that their next step was to test the stability of the particles in suspension at geothermal conditions. A third type of particle tracer called Temperature-Time Tracers (TTTs) was modeled, capable of measuring and recording detailed temperature-time histories encountered by each tracer particle. Practical TTTs do not exist, but would represent the most sophisticated particle tracer imaginable (short of particles that communicate their position and temperature to the surface wirelessly and in real time), and it is hypothesized that these tracers represent the upper bound of informativity about thermal breakthrough. The existing tracers that were modeled are Conservative Solute Tracers (CSTs), reactive solute tracers (RSTs), and Sorbing Solute Tracers (SSTs). Gas-phase tracers are also used in vapor-dominated geothermal reservoirs, but only tracers dissolved in the liquid phase were considered here for simplicity. A general model was written in MATLAB to account for all six tracer types described above, and compiled to interface it with the optimization algorithm used. This tracer model was dubbed **T**hermally **R**esponsive tr**A**cer **C**od**E**, or TRACE.

2.1 Linear Pressure Model

It is useful to represent a fracture network as a "graph", consisting of edges (fractures) and nodes (wells and fracture intersections). The flowrates and travel times along each edge are inputs to the tracer models, so the node pressures must first be calculated. The following model was used as a proxy for reservoir simulation to solve for node pressures. First, all fractures are split at the wells and at intersections. Then, all fractures that are not connected directly or indirectly to a well are removed from consideration. Finally, dead end fractures are removed from consideration and a list of nodes and segments is built for the remaining fractures.

This model uses the analytical solution for Poisueille flow between parallel plates. The flow along edge j from nodes i to node h is described in Equation 1.

$$Q_j = \frac{W_j {b_j}^3}{12\mu L_j}(p_h - p_i) + Q_{WELL,j} = C_j(p_h - p_i) + Q_{WELL,i} \quad (1)$$

where Q_j, W_j, b_j, and L_j are the flowrate, fracture width, fracture aperture, and fracture length of edge j; μ is fluid viscosity; p_h and p_i are the pressures at nodes h and i; and $Q_{WELL,i}$ is the well flowrate at node i (if one exists), respectively. If no well exists at node i, $Q_{WELL,i} = 0$. C_j represents the grouping of all the fracture and fluid parameters into a constant term.

The production well pressure was chosen to be specified, and the production flowrate was set as an unknown. It was assumed that fluid viscosity and density are both constant everywhere in the fracture network. In order to ground the pressure magnitude, one pressure

must be specified. This enabled us to use linear algebra to directly solve for all unknowns (i.e. node pressures and production well flowrate) by setting up the system of linear mass balance equations shown in Equation 2.

$$\overline{\overline{\boldsymbol{T}}}\bar{\boldsymbol{p}} = \bar{\boldsymbol{r}} \tag{2}$$

where $\overline{\overline{\boldsymbol{T}}}$, $\bar{\boldsymbol{p}}$, and $\bar{\boldsymbol{r}}$ are the matrix containing the relevant values of C_j for each node (see Equation 1), the vector of unknowns (node pressures and production well flowrate), and the right-hand side vector, which contains constant terms corresponding to the injection well flowrate and the production well pressure term, respectively. The right-hand side contains zeros at all nodes except for nodes on rows corresponding to nodes that contain wells or are adjacent to well nodes.

An example pressure field calculated in this way is given in Figure 1. The parameter values used in Figure 1 are shown in Table 1.

Table 1: Linear pressure model parameter values.

Parameter	Value	Units
Q_{inj}	0.005	$\frac{\mathrm{m}^3}{\mathrm{s}}$
p_{prod}	18	MPa
μ	1.87×10^{-4}	Pa-s
W	250	m
b	$6.9 \times 10^{-4} L^{0.41}$	m

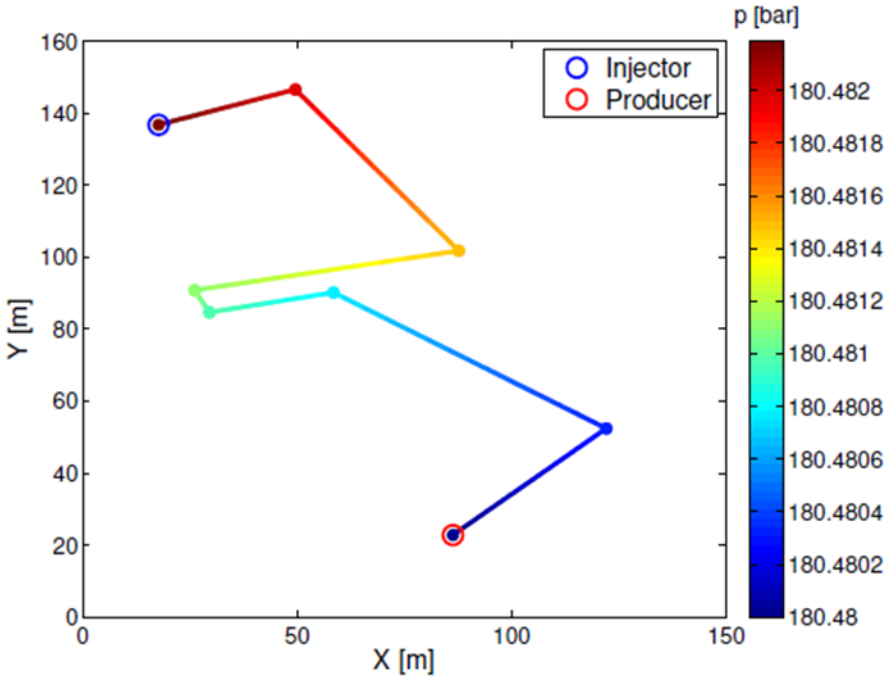

Figure 1: Illustration of linear pressure model for discrete fracture networks.

Once the pressures at each node are known, the edge flowrates and travel times can be calculated using the cubic law (Equation 3) and the equation for residence time (Equation 4).

$$Q_j = \frac{W_j {b_j}^3}{12\mu L_j}(p_h - p_i) \tag{3}$$

$$\tau_j = \frac{V_j}{Q_j} = \left(\frac{LWb}{Q}\right)_j \tag{4}$$

where τ_j and V_j are the travel time and volume of edge j, respectively. All other parameters are as defined previously.

The main drawback of this linear proxy model is that there is some approximation error in the calculated pressure, flowrate, and travel time due to the assumption of constant viscosity, density, no matrix flow, and no rock compressibility. However, it is worth using this model for its large increase in computational efficiency.

2.2 Analytical Temperature Model

In order to model thermally responsive tracers in discrete fracture networks, it was first required to calculate the reservoir temperature field at the time of the tracer test. This can be calculated numerically using a reservoir simulator, but a more computationally efficient model was desired in order to make inverse search feasible. Fox (2016) derived an analytical model for temperature in a discrete fracture network where reinjection is occurring at a constant flowrate, given in Equations 5 to 10. This model uses successive convolution to account for the complex effects of flowpath mixing and splitting at fracture intersections. The successive convolution model is based on the solution for a single fracture (Equation 5), in which it is assumed that injection and production rates are equal and conduction is only significant in the dimension perpendicular to flow.

$$\Theta(x,y,t) = \frac{T_w(x,t)-T_{inj}}{T_{res}-T_{inj}} = \operatorname{erf}\left(\frac{1}{2}\frac{y+\beta x}{\sqrt{\alpha\left(t-\frac{x}{v}\right)}}\right) \tag{5}$$

where x, y, t, $\Theta(x,y,t)$, T_{res}, T_{inj}, α, β, and v are position along the axis of flow, position along the axis perpendicular to flow, time since injection began, dimensionless temperature as a function of time and position, original reservoir temperature before injection, temperature of injected fluid, thermal diffusivity of reservoir rock which is defined in Equation 6, a dimensionless lumped parameter which is defined in Equation 7, and average interstitial fluid velocity.

$$\alpha = \frac{K_r}{\rho_r C_r} \tag{6}$$

$$\beta = \frac{2K_r}{\rho_w C_w v b} = \frac{2K_r W}{\dot{m} C_w} \tag{7}$$

where K_r, ρ_r, and C_r are the thermal conductivity, density, and heat capacity of the reservoir rock, ρ_w and C_w are the density and heat capacity of the fluid, and $\dot{m}$, b, and W are injection mass flowrate, fracture aperture, and fracture width (i.e. reservoir thickness when fractures have a vertical orientation and extend through the whole reservoir thickness).

If temperature is calculated at the fracture centerline $y = 0$, the variable y falls out of the equation. Furthermore, it is reasonable to assume that $\frac{x}{v} \ll t$ on the spatial and time scales of interest. This simplifies the equation for temperature in a single fracture to Equation 8.

$$\Theta(x,t) = \operatorname{erf}\left(\frac{1}{2}\frac{\beta x}{\sqrt{\alpha t}}\right) \tag{8}$$

Fox (2016) derived the temperature in a discrete fracture network as the successive convolution of the simplified single fracture solution (Equation 8), resulting in Equations 9 and 10. An inherent assumption in this model is there is no thermal interference between fractures. This assumption breaks down when fracture spacings are sufficiently small.

$$\Theta_k(x,t) = \sum_{p=1}^{N_p} \prod_{j\in S_p} \chi_j \operatorname{erf}\left(\frac{1}{2}\frac{\beta_k x}{\sqrt{\alpha t}} + \sum_{j\in S_p} \frac{1}{2}\frac{\beta_j L_j}{\sqrt{\alpha t}}\right) \tag{9}$$

$$T_k(x,t) = T_{inj} + \left(T_{res} - T_{inj}\right)\Theta_k(x,t) \tag{10}$$

where p represents a path from the injection well to fracture segment k, N_p is the number of such paths, S_p is the set of fracture segments in path p, j is the index referencing these segments, χ_j is the fraction of the mass flowrate along segment k that is contributed by segment j, x is the position along segment k where the temperature is calculated, and L_j is the length of segment j.

Equations 9 and 10 were used to calculate all temperature fields in the inverse analysis of discrete fracture networks. Fractures were not only broken into segments at intersections, but also further subdivided into elements in order to capture the temperature field in higher resolution, as shown in Figure 2. The thermal breakthrough curve at the production well calculated for the same network using this model is given in Figure 3. Model parameter values used in Figure 2 and Figure 3 are given in Table 2.

Table 2: Analytical temperature model parameter values.

Parameter	Value	Units
T_{inj}	100	°C
T_{res}	200	°C
ρ_w	926.6	$\frac{\text{kg}}{\text{m}^3}$
C_w	4254	$\frac{\text{J}}{\text{kg°C}}$
K_r	3.3	$\frac{\text{W}}{\text{m°C}}$
ρ_r	2700	$\frac{\text{kg}}{\text{m}^3}$
C_r	1050	$\frac{\text{J}}{\text{kg°C}}$
t_{test}	200	days

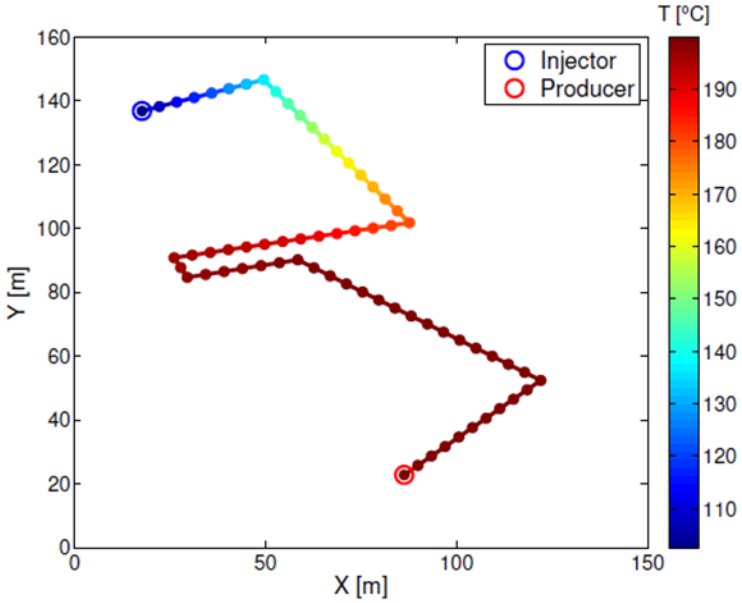

Figure 2: Example temperature field calculated using analytical temperature model for discrete fracture networks.

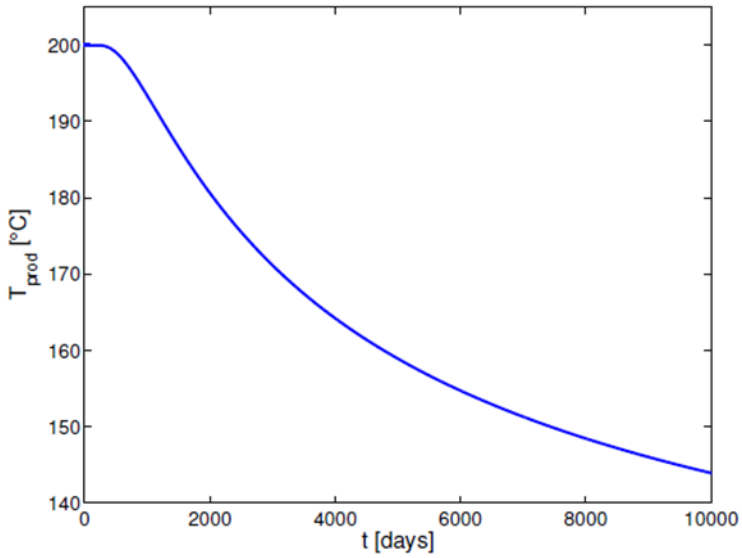

Figure 3: Example of thermal breakthrough curve calculated using analytical temperature model.

2.3 General Tracer Model

Tracer tests are commonly performed to characterize geothermal fields. Tracers are injected into injection wells, and the production wells are monitored over time for tracer arrival. The tracer concentration measured over time is referred to as a return curve or breakthrough curve, and this is the data that is used to attempt to characterize the reservoir properties quantitatively. A method derived by Juliusson (2012) for calculating tracer returns in a fracture network using successive convolution in Laplace space was used in this work. First, a depth first search was performed to determine all unique paths from the injection well to production well in the fracture network. Then, successive convolution of tracer kernels was performed in Laplace space (see Equations 12 through 21). Finally, the result of Equation 12 was inverted numerically in Equation 11 using the Den Iseger algorithm to obtain the return curves (den Iseger 2006). With permission from the author, TRACE uses the MATLAB routine for the Den Iseger algorithm developed by Juliusson (2010), which was slightly modified in TRACE to vectorize input times and increase computational efficiency. This method has the advantage of being numerically efficient compared to reservoir simulation (except for fracture networks with a large number of inter-well paths), and it does not suffer from numerical dispersion. Performing the successive convolution in Laplace space and numerically inverting the result is especially efficient because convolution is equivalent to simple multiplication in Laplace space. Juliusson (2012) performed a comparison study which showed that the Den Iseger algorithm is more robust for this application than the Stehfest algorithm.

Tracer return curves for complex fracture networks were calculated using Equation 11.

$$c(t) = \mathcal{L}^{-1}\{C(s)\} = \mathcal{L}^{-1}\left\{\sum_{p=1}^{N_p} C_p(s)\right\} \tag{11}$$

where $c(t)$, $\mathcal{L}^{-1}$, $C_p(s)$, N_p, and s are the tracer concentration observed at the production well as function of time, inverse Laplace transform, the tracer concentration contribution of path p observed at the production well as a function of time in Laplace space (defined in Equation 12), the number of unique inter-well flowpaths in the fracture network, and the Laplace transform variable, respectively.

$$C_p(s) = \frac{m_{inj}}{Q_{inj}} \prod_k^{K(p)} \frac{q_k}{\sum_j^{J(k)} q_j} \prod_k^{K(p)} \widetilde{\kappa_k}(s) \tag{12}$$

where k runs over all $K(p)$ edges on path p, j runs over all $J(k)$ edges with outflow from the source node of edge k, and m_{inj}, Q_{inj}, q_k, and $\widetilde{\kappa_k}(s)$ are the tracer mass in the injected slug, the steady-state volumetric flowrate of injection during tracer slug injection, the flowrate along edge k, and Laplace transform of the tracer kernel function for a unit impulse, respectively.

General tracer kernel functions were derived for both solute and particle transport. Solute tracers considered include conservative solute tracers (or CSTs), reactive solute tracers (or RSTs), and sorbing solute tracers (or SSTs). For this reason, a general solute tracer model was derived accounting for advection, dispersion, reaction, and sorption based on similar derivations by Maloszewski and Zuber (1983), Reimus et al. (2003), and Humphrey et al. (2001). This solute tracer model is shown in Equations 13 through 16.

$$\widetilde{\kappa_k}(s) = \bar{C}_{sol}(s) = \exp\left(\frac{v_k L_k}{2D_L}\left(1 - \sqrt{1 + \frac{4D_L}{{v_k}^2}\left(\frac{2\phi_m}{b_k \phi_f}\sqrt{\mathcal{D}_{m,k} R_{m,k}(s)} + R_{f,k}(s)\right)}\right)\right) \tag{13}$$

$$R_{f,k}(s) = \lambda_k + s\left(1 + \frac{2K_{a,k}}{b_k}\right) \tag{14}$$

$$R_{m,k}(s) = \lambda_k + s\left(1 + \rho_m\left(\frac{1+\phi_m}{\phi_m}\right)K_{d,k}\right) \tag{15}$$

$$K_{d,k} = (SSA)K_{a,k} \tag{16}$$

where $\bar{C}_{sol}(s)$, D_L, ϕ_m, and ϕ_f are the tracer kernel for solute tracers along edge k in Laplace space, longitudinal dispersivity, matrix porosity, and fracture porosity, respectively and v_k, L_k, b_k, $\mathcal{D}_{m,k}$, $R_{f,k}(s)$, $R_{m,k}(s)$, λ_k, $K_{a,k}$, $K_{d,k}$, and SSA are the average interstitial fluid velocity, fracture length, fracture aperture, matrix diffusivity of the solute, a lumped term for retardation and reaction in the fracture, a lumped term for retardation and reaction in the matrix, reaction rate coefficient, fracture partition coefficient, matrix partition coefficient, and specific surface area along edge k, respectively.

Reimus et al. (2007) used experimental data to develop a correlation between the ratio of matrix diffusivity to diffusivity in free water $\frac{\mathcal{D}_m}{\mathcal{D}_{sol}}$ and matrix porosity ϕ_m. The slightly modified version of this correlation reported by Williams et al. (2013) was used to calculate $\mathcal{D}_m$ in this work (Equation 17).

$$\mathcal{D}_{m,k} = \mathcal{D}_{sol,k} 10^{3.0681\phi_m - 1.979} \tag{17}$$

where $\mathcal{D}_{m,k}$ and $\mathcal{D}_{sol,k}$ are the temperature dependent matrix and free water diffusivities along edge k. The diffusivity in free water $\mathcal{D}_{sol}$ increases with temperature, and this effect is enhanced by the fact that the viscosity of water μ decreases with temperature. The expression that describes both of these effects used by Williams et al. (2013) was used in this work (Equation 18). Additionally, the

experimental correlation for the temperature dependence of the viscosity of water reported by Likhachev (2003) was used (Equation 19).

$$\frac{\mathcal{D}_{sol}}{\mathcal{D}_{sol,298K}} = \frac{T_{abs}}{298}\frac{\mu_{298K}}{\mu(T_{abs})} \tag{18}$$

$$\mu(T_{abs}) = 2.4152 \times 10^{-5} \exp\left(\frac{4742.8}{R(T_{abs}-139.86)}\right) \tag{19}$$

where T_{abs}, $\mu(T_{abs})$, μ_{298K}, and R are the absolute temperature, water viscosity as a function of temperature, water viscosity at $T = 298\ K$, and ideal gas constant, respectively. Finally, Arrhenius kinetics were assumed for the decay reaction, as described in Equation 20.

$$\lambda_k = A_R \exp\left(-\frac{E_A}{RT_{abs,k}}\right) \tag{20}$$

where A_R and E_A are the Arrhenius pre-exponential factor and activation energy of the reaction, respectively.

Particle tracers considered include dye-releasing tracers (DRTs), threshold nano-reactor tracers (TNRTs), and temperature-time tracers (TTTs). Particle tracers in porous and fractured media which experience minimal deposition tend to move more rapidly than the average fluid velocity and experience breakthrough sooner than solute tracers, which is likely due to colloids being too large to experience matrix diffusion and their tendency to stay in high velocity fluid streamlines (Reimus 1995, Becker et al. 1999). Thus, when modeling particle transport, matrix diffusion was neglected ($\phi_m = 0$), as well as reaction ($\lambda_k = 0$) and sorption ($K_{a,k} = 0$ and $K_{d,k} = 0$), causing Equation 13 to reduce to Equation 21, which is a solution to the classical advection-dispersion equation in Laplace space.

$$\widetilde{\kappa_k}(s) = \bar{C}_{np}(s) = \exp\left(\frac{L_k}{2D_L}\left(v_{eff,k} - \sqrt{{v_{eff,k}}^2 + 4D_L s}\right)\right) \tag{21}$$

where $\bar{C}_{np}(s)$ and $v_{eff,k}$ are the tracer kernel for particle tracers and the particle velocity along edge k in Laplace space. The particle velocity $v_{eff,k}$ is calculated using Equation 22, which is an analytical solution for the effective average particle velocity derived by James and Chrysikopoulos (2001). This equation accounts for the exclusion of particles from slower streamlines due to the particles being excluded from a region the size of the particle diameter in the dimension of the fracture aperture.

$$v_{eff,k} = v_k\left(1 + \frac{d_p}{b_k} - \frac{1}{2}\left(\frac{d_p}{b_k}\right)^2\right) \tag{22}$$

where v_k is the average interstitial velocity along edge k, d_p is particle diameter, and b_k is fracture aperture in edge k.

The difference between the return curves for solutes and particles is illustrated in Figure 4. The particle tracer breaks through slightly earlier than the solute tracer, while the solute tracer return curve has a longer tail. This difference is primarily due to the fact that the solute tracer experiences matrix diffusion, while the particle tracer does not. Particle exclusion from fracture walls also causes particles to breakthrough slightly earlier than solutes, but this effect is noticeable only when $\frac{d_p}{b_k}$ is sufficiently large.

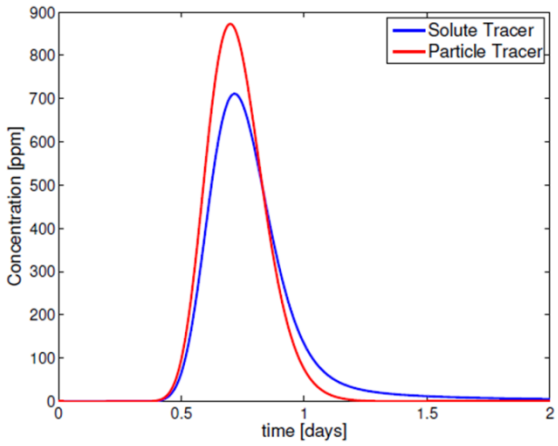

Figure 4: Comparison of solute and particle tracer return curves.

TNRT return curves were calculated differently than all other tracer types. A random-walk particle tracking model which accounts for dispersion was used to calculate temperature-time histories of 10,000 representative tracer particles, which was then used to calculate the extent of reaction using Equation 23 and return curves for various temperature thresholds using Equation 24.

$$1 - \xi(t) = \exp\left(\int_0^t \lambda(\tau)\, d\tau\right) = \exp\left(\int_0^t A_R \exp\left(-\frac{E_A}{R}\frac{1}{T_{abs}(\tau)}\right) d\tau\right) \tag{23}$$

where $\xi(t)$ is the extent of reaction within the nanoreactor at time t, $\lambda(\tau)$ is the reaction rate constant at a specified time in the particle's history, τ is a dummy variable for time t, and $T_{abs}(\tau)$ is absolute temperature at a specified time in the particle's history.

$$c_A(t) = \left(1 - \bar{\xi}(t)\right) c(t) \tag{24}$$

where $c_A(t)$ is the TNRT return curve for a given threshold temperature, $1 - \bar{\xi}(t)$ is the average fraction of reactant A remaining in the particles at residence time t, and $c(t)$ is the return curve concentration of nanoreactor particles calculated by plugging the particle kernel (Equation 21) into Equations 11 and 12. The term $1 - \bar{\xi}(t)$ is calculated as the average of the reactant fraction values for individual particles within each residence time bin in the return curve.

TTTs were also modeled differently than other tracer types. Ames and Horne (2014) showed that detailed temperature-time histories can be used to infer fracture network topology including flowrates, travel times, and temperatures. It is useful to represent this information as a directed graph where edges correspond to fracture flowpaths and nodes correspond to wells and fracture intersections. The information provided by TTT tracer tests was modeled by reducing the fracture network to a graph including information flowrates, travel times, and temperatures. In the inverse problem cases described in this work, this graph was matched in addition to the TTT return curve, which was calculated using the particle kernel (Equation 21).

Tracer parameter values used in this work that are shared by all tracer types are given in Table 3, and parameter values specific to each tracer type are given in Table 4 through Table 9.

Table 3: Tracer model parameter values.

Parameter	Value	Units
D_L	0.02	$\frac{\mathrm{m}^2}{\mathrm{s}}$
ϕ_m	0.1	-
ϕ_f	1	-
$\mathcal{D}_{sol,298K}$	5×10^{-10}	$\frac{\mathrm{m}^2}{\mathrm{s}}$

Table 4: CST model parameter values.

Parameter	Value	Units
K_a	0	$\frac{\mathrm{m}^3}{\mathrm{m}^2}$
SSA	n/a	-
A_R	0	s^{-1}
E_A	n/a	-
d_p	n/a	-

Table 5: RST model parameter values.

Parameter	Value	Units
K_a	0	$\frac{\mathrm{m}^3}{\mathrm{m}^2}$
SSA	n/a	-
A_R	1.6×10^7	s^{-1}
E_A	1.07×10^5	$\frac{\mathrm{J}}{\mathrm{mol}}$
d_p	n/a	-

Table 6: SST model parameter values.

Parameter	Value	Units
K_a	1×10^{-5}	$\frac{\mathrm{m}^3}{\mathrm{m}^2}$
SSA	350	$\frac{\mathrm{m}^2}{\mathrm{kg}}$
A_R	0	s^{-1}
E_A	n/a	-
d_p	n/a	-

Table 7: DRT model parameter values.

Parameter	Value	Units
K_a	0	$\frac{\mathrm{m}^3}{\mathrm{m}^2}$
SSA	n/a	-
A_R	0	s^{-1}
E_A	n/a	-
d_p	100	nm

Table 8: TNRT model parameter values.

Parameter	Value	Units
K_a	0	$\frac{\mathrm{m}^3}{\mathrm{m}^2}$
SSA	n/a	-
A_R	1.6×10^7	s^{-1}
E_A	1.07×10^5	$\frac{\mathrm{J}}{\mathrm{mol}}$
d_p	100	nm

Table 9: TTT model parameter values.

Parameter	Value	Units
K_a	0	$\frac{\mathrm{m}^3}{\mathrm{m}^2}$
SSA	n/a	-
A_R	0	s^{-1}
E_A	n/a	-
d_p	100	nm

Some of the parameters in the tracer kernel are temperature dependent (e.g. λ_k), which requires breaking fracture edges further into discrete fracture elements in order to model the tracer returns on the same grid as the temperature field. The successive convolution model can be extended readily to account for this. In this case, the index k in Equations 11 through 22 refers to element ID rather than edge ID. For further modeling details, please refer to Ames (2016).

2.4 Inverse Problem

A framework was constructed to solve the mixed-integer nonlinear programming (MINLP) optimization problem of matching tracer data in discrete fracture networks with a variable number of fractures. The problem is mixed-integer because some of the decision variables are both integer valued (i.e. a binary decision variable to turn each fracture "on" or "off") and continuous (i.e. fracture location, length, and orientation). The problem is a nonlinear programming problem because both the objective function and constraints are nonlinear. A derivative-free optimization algorithm called PSO-MADS was chosen, and an algorithm was developed to handle disconnected fracture networks using a constraint. This is well-suited for this particular modeling approach because the solution space is mostly populated with fracture networks in which the wells are not connected, and the forward model requires the wells be connected by fractures. For this reason, disconnected fracture networks are considered infeasible but are connected by adding fractures in a recursive approach. The sum of the lengths of the added fractures is the constraint violation value, which is minimized as an additional objective.

2.4.1 Inverse Problem Formulation

The tracer inverse problem in this work is formulated in Equations 25 and 26.

$$\min_{\boldsymbol{m}\in M} f(\boldsymbol{m}) \tag{25}$$

subject to:

$$h(\boldsymbol{m}) \leq 0 \tag{26}$$

where $\boldsymbol{m}$ is the vector of decision variables that describe the fracture network, M is the set of all possible values of $\boldsymbol{m}$, $f(\boldsymbol{m})$ is the objective function to be minimized, and $h(\boldsymbol{m})$ is the nonlinear constraint violation that measures how disconnected a fracture network is.

2.4.2 Decision Variables

The decision variables to be used in optimization were formulated such that the number of fractures in the network is allowed to vary between two and ten fractures. The decision variables for each fracture are a binary variable determining whether a fracture was turned "on" or "off", fracture center point x- and y-coordinates, fracture orientation, and fracture length. In order to guarantee that at least one fracture intersected each well, two fractures (the "well fractures") are formulated differently. First, well fractures not given the flexibility to be turned "on" or "off" in order to ensure that well fractures exist in all candidate networks. Second, as they are required to intersect a fixed well location, only three parameters are required to define them: length, orientation, and the fractional distance along the fracture between the center point and the well. In general, the number of decision variables for this formulation is given by Equation 27.

$$N_{DV} = 5(N_F - N_W) + 3N_W \tag{27}$$

where N_{DV} is the total number of decision variables, N_F is the maximum number of fractures considered, and N_W is the number of wells, respectively. For example, a maximum of 10 fractures corresponds to a total of 46 decision variables.

Rather than allowing aperture to vary freely as a decision variable in the optimization, it was decided to calculate the aperture of each fracture as a function of its length. This was done for two reasons. First, this reduces the number of decision variables by the maximum number of fractures N_F, which reduces the difficulty of the inverse search. Secondly, researchers have reported that fracture aperture and length are correlated, citing both field observations and fracture mechanics theory (Olson 2003). Olson (2003) performed a survey of aperture values reported in literature and included power law correlations for both dikes, which have very large apertures relative to their lengths, and mineralized veins, which have much smaller apertures relative to their lengths. These correlations are in the form shown in Equation 28. To be consistent with the Enhanced Geothermal Systems concept, the related modeling assumptions, and the fractured granite outcrop used to generate the true fracture networks (see Section 2.4.6), the correlation for mineralized veins at Florence Lake was used, which is shown in Equation 29. This was the most consistent with the fractured granite assumption because the veins at Florence Lake were in a granodiorite body, which is similar to granite.

$$b = CL^e \tag{28}$$

$$b = 6.9 \times 10^{-4} L^{0.41} \tag{29}$$

where b is fracture aperture, L is fracture length, C is a pre-exponential constant, and e is a scaling exponent for the power law correlation.

2.4.3 Objective Function

The objective function to be minimized is defined for all tracer types (except for TTTs) in Equation 30.

$$f(\boldsymbol{m}) = f_{RC}(\boldsymbol{m}) + f_{RT}(\boldsymbol{m}) \tag{30}$$

where $f(\boldsymbol{m})$, $f_{RC}(\boldsymbol{m})$, and $f_{RT}(\boldsymbol{m})$ are the objective function, the component of the objective function measuring the fitness of the return curves, and the component of the objective function measuring the fitness of the peak residence times, respectively.

The return curve component of the objective function $f_{RC}(\boldsymbol{m})$ is a metric of how well a given model curve fits the data. This is often the only component of the objective function used in curve fitting optimization problems, and it is often calculated as a simple Euclidean distance. In this work, it was calculated as the integral of the difference between the return curves for the model and the data, normalized by the area under the data return curve. This particular formulation was chosen because it was easier to normalize than a simple Euclidean distance (normalization is necessary in this case because there are multiple components of the objective function that contain different metrics) and because the time series in the synthetic return curve data were not always evenly spaced (which would make a Euclidean distance a less accurate metric of curve fitness).

Rather than simply formulating the objective function as the return curve component described in the previous section, another component was added to account for the time difference between return curve peaks, which is referred to as $f_{RT}(\boldsymbol{m})$ in Equation 30. This was done to mitigate the problem of a flat objective function surface for candidate networks with very little or no overlap with the data return curve. In this case, the area between the curves is roughly equal to the sum of the areas under both curves, regardless of the distance between the curves on the time axis, which would result in a flat objective function surface for curves that have no overlap with the data. The peak residence time component of the objective function introduces a slope to the objective function surface by penalizing

curves more the farther their peaks are from the peak of the data return curve. This is calculated as the normalized difference between the peak arrival time of the model and data return curves.

The objective function for the TTT has an additional component in its objective function called graph edit distance, which is a heuristic graph dissimilarity metric (see Equation 31). This enabled the matching of flowpath topology, path flowrates, travel times, and temperatures inferred from TTT data.

$$f(\boldsymbol{m}) = f_{RC}(\boldsymbol{m}) + f_{RT}(\boldsymbol{m}) + f_{ED}(\boldsymbol{m}) \tag{31}$$

where $f_{ED}(\boldsymbol{m})$ is the edit distance between the two graphs and all other parameters are previously defined. Edit distance was calculated using the method developed by Riesen and Bunke (2009), which is based on the Hungarian algorithm (Kuhn 1957 and Munkres 1957). Further details about the formulation of each component of the objective function can be found by referring to Ames (2016).

2.4.4 Nonlinear Constraint Violation

Because no matrix flow is considered, the forward models require that the injection and production wells be connected by fractures. An algorithm was developed to connect fracture clusters recursively until the wells are connected, so that the objective function of infeasible solutions could be approximated (see Algorithm 1).

Algorithm 1: Recursive fracture cluster connection algorithm

while *the wells are not connected by fractures:*

1. *Group all fractures into isolated clusters of connected fractures.*
2. *Add a "virtual fracture" corresponding to the minimum distance between fracture clusters.*

A graphical illustration of this algorithm is given in Figure 5.

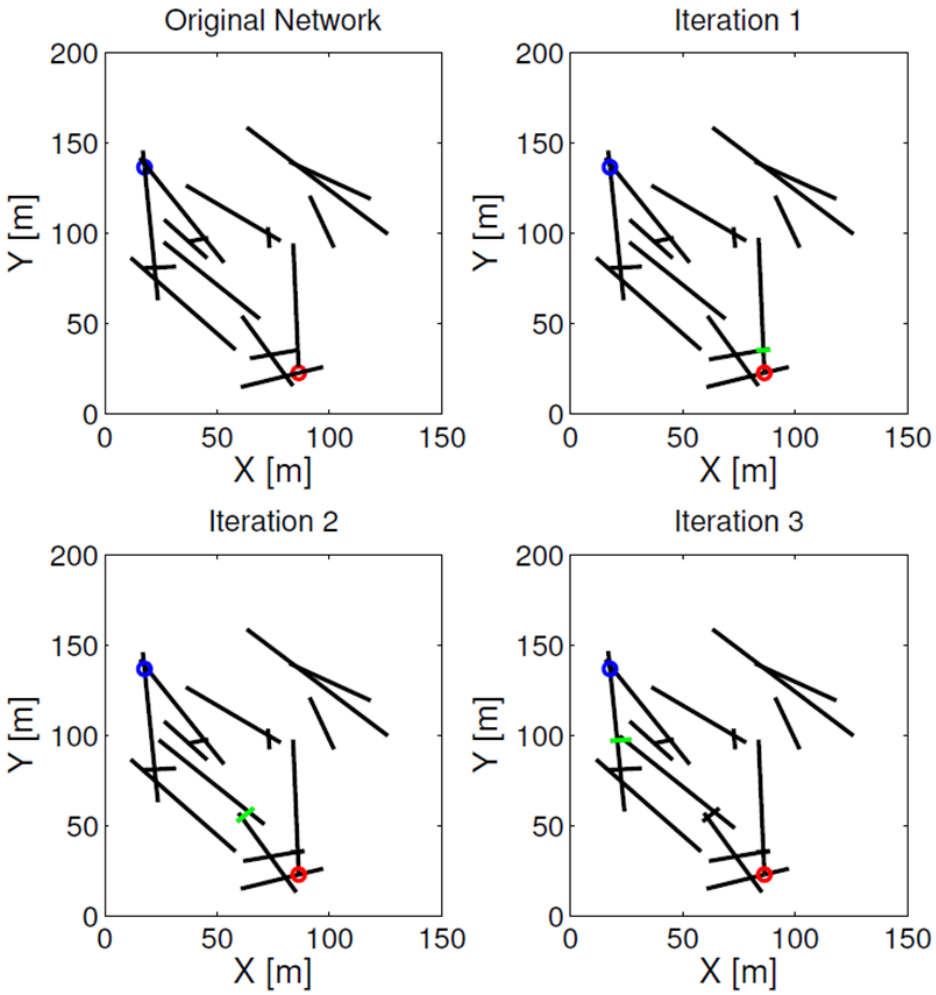

Figure 5: Graphical illustration of recursive fracture cluster connection algorithm for the originally disconnected network with the newest virtual fracture at each iteration highlighted in green.

The constraint value used was simply the sum of the lengths of fractures that needed to be added to connect the wells. This method was designed to both guide the optimization algorithm toward feasible regions of the search space and to utilize objective function approximations for infeasible solutions to aid in the optimization. For example, if a fracture network is infeasible but would be a good match if one of the fractures were slightly longer, the objective function approximation would be low, which helps inform the optimization algorithm to move in that search direction.

2.4.5 PSO-MADS Optimization Algorithm

Fracture networks that are not connected in this way are considered infeasible solutions to the inverse problem. An optimization algorithm called PSO-MADS was used to search the optimization space (Isebor 2013, Isebor et al. 2014a, and Isebor et al. 2014b). PSO-MADS is a hybrid of Particle Swarm Optimization (PSO), a stochastic global search method, and Mesh Adaptive Direct Search (MADS), a local pattern search method. This algorithm is derivative-free, can handle integer problems, and is capable of handling infeasible solutions by using a constraint violation. Only feasible solutions can be considered optimal, but the constraint violation value can be used to guide the algorithm toward feasible solutions.

2.4.6 True Fracture Networks

The true fracture networks used to generate synthetic tracer data were based on a real fractured granite outcrop in the Catalan Costal Ranges of Spain, called the Tamiaru outcrop. Place et al. (2011) used this outcrop as an analog to study the fluid flow patterns in the Soultz-sous-Forets EGS project. Based on observations of a network of carbonate veins in the Tamiaru outcrop, it is believed that this network hosted fluid flow in the past, and the outcrop is considered a fossil geothermal reservoir. This outcrop was chosen as a basis for the true fracture networks because it was mapped in aerial view, at the appropriate scale, and is in fractured granite, which is consistent with the rock properties and associated modeling assumptions.

The Tamiaru fractured granite outcrop was used as a starting point for all true fracture networks in this study. A section the fracture outcrop was chosen as an area of focus for this study, as shown in the aerial image reproduced from Place et al. (2011) in Figure 6. Then, 100 fractures in a subsection of the outcrop were manually digitized. However, the 100 fracture case was not computationally feasible as a true case in this study for two reasons. First, the optimization problem would have 496 decision variables, meaning optimizations would require a very large number of objective function evaluations to explore the objective function surface sufficiently. Second, a single objective function evaluation for the 100 fracture problem is prohibitively expensive computationally. In order to preserve as much realism in this fracture network as possible while reducing the number of fractures, the maximum flowrates along all the segments of each individual fracture were calculated, and the fractures were ranked according to their maximum flowrates. Next, three fracture networks with 7, 9, and 15 fractures were constructed by removing all of the digitized fractures except for those with the highest flowrates (see Figure 7). This was done somewhat heuristically, because several of the 30 highest ranked fractures were disconnected from the others, in which case a lower ranked fracture was used in its place.

These three fracture networks were used as true fracture networks in inverse problems to examine whether the complexity of the flow topology affects the informativity of each tracer. The fact that each network shares the same basic character originating from a real fractured outcrop made it possible to isolate the effect of flow complexity from other potential factors such as the geometric shape of the fracture network (since all of the fracture networks have the same basic shape). Each true network also represents a different type of thermal behavior, all of which are possible for the well configuration considered. The 7 fracture network represents a short circuit, and the 9 fracture network and 15 fracture network each represent a more efficient thermal sweep than the previous network (see Figure 8).

The fracture network parameter values that were used are given in Table 10. The longest fracture in the digitized fracture network is 83.6 meters, so it was decided to set the range of possible fracture lengths in optimizations at 1 to 100 meters. The value of longitudinal dispersivity that was used $\left(D_L = 0.02\frac{m^2}{s}\right)$ was based on values inferred from a large number of tracer tests compiled by Zhou et al. (2007). Finally, the digitized fracture network was used to generate semi-random starting points for the optimization. Starting point fracture networks were generated stochastically by sampling cumulative distribution functions built from the orientations, lengths, and center point coordinates of the fractures in the digitized network.

Table 10: Fracture network parameter values used in this study.

Parameter	Value	Units
X_{res}	160	m
Y_{res}	160	m
W	250	m
L	1 to 100	m
b	$6.9 \times 10^{-4} L^{0.41}$	m
D_L	0.02	$\frac{\mathrm{m}^2}{\mathrm{s}}$

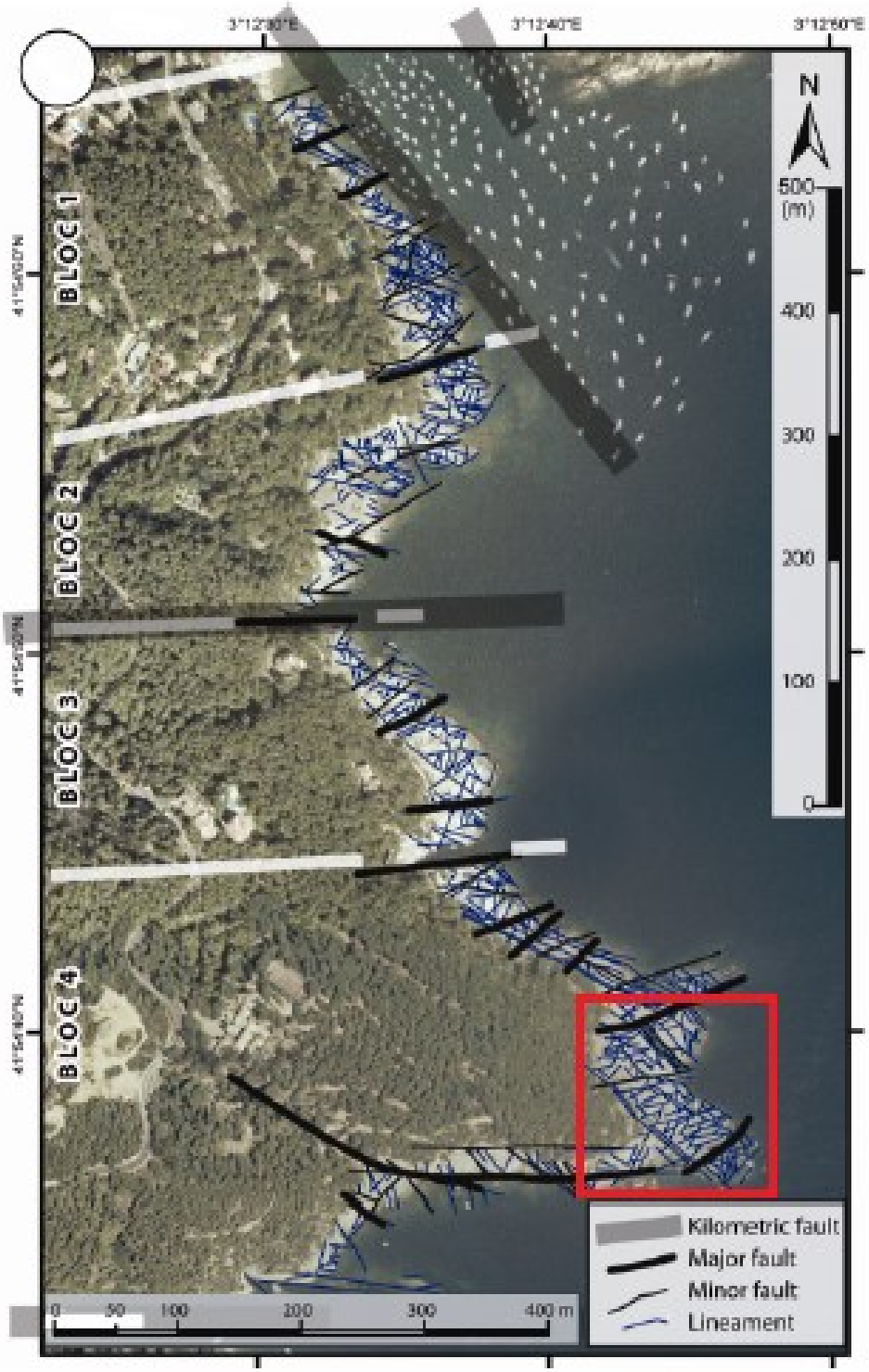

Figure 6: Full aerial image of Tamiaru fractured granite outcrop reproduced from Place et al. (2011) with a red box drawn around part of the outcrop that was used for this study.

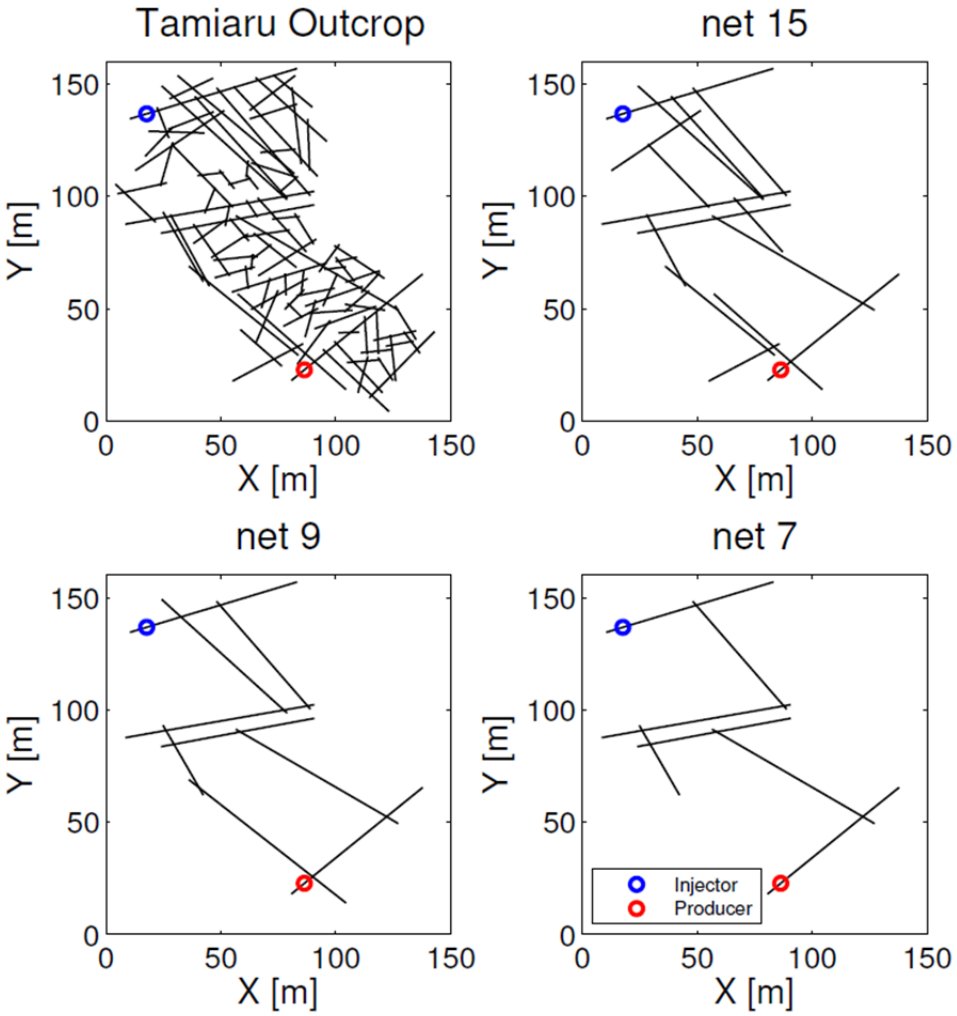

Figure 7: Digitized network with 100 fractures based on the Tamiaru Outcrop and the simplified true fracture networks with 15, 9, and 7 fractures.

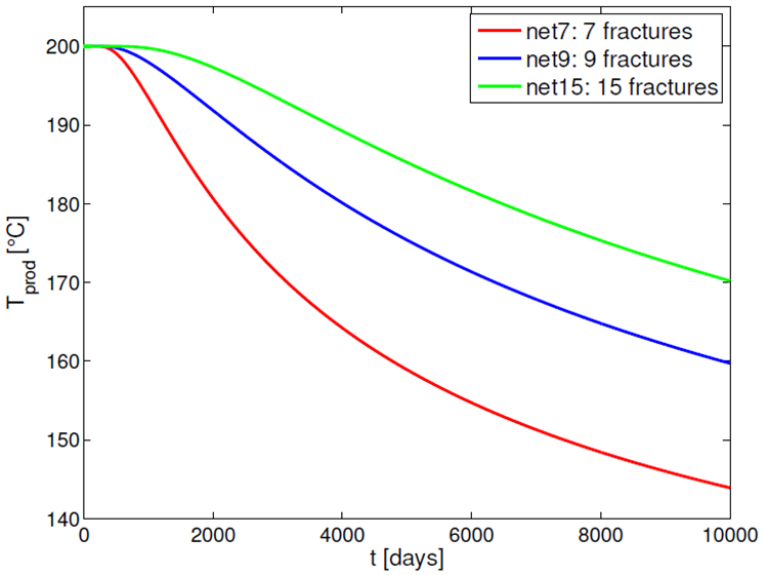

Figure 8: Thermal breakthrough curves of true fracture networks.

3. RESULTS

Discrete fracture network optimizations were performed to match synthetic tracer data for six tracer types (CST, RST, SST, DRT, TNRT, and TTT) and three different true fracture networks of increasing complexity (net 7, net 9, and net15). Each optimization was repeated a number of times with different stochastically generated starting points, and the best solution from the repetitions was taken as the optimum. The number of repetitions required to find an acceptable fit to the synthetic tracer data varied with the complexity of the true fracture network.

Thermal breakthrough forecasts were calculated for optimal fracture networks found for each tracer type and true fracture network, and these forecasts were compared to the thermal breakthrough behavior of the corresponding true fracture networks. The error of each thermal breakthrough forecast was quantified using two types of metrics, and the tracers were ranked in order of forecast accuracy for each true fracture network. The first thermal breakthrough forecast error metric is dubbed Thermal Breakthrough Area Difference ($TBAD$), the normalized absolute difference between the forecasted thermal breakthrough curve and the true thermal breakthrough curve, as described in Equation 32. The second metric is dubbed Percent Time Difference ($PTD_{x°C}$), the percent error in predicting the time of a specified drop in temperature, as described in Equations 33 to 35. Three specified temperature drops were used here: 10°C, 20°C, and 25°C.

$$TBAD = \frac{\int_{t=0}^{t=t_{end}} |T_{prod,MOD}(t) - T_{prod,TRUE}(t)|\, dt}{\int_{t=0}^{t=t_{end}} |T_{prod,TRUE}(t) - 100°C|\, dt} \times 100\% \tag{32}$$

where $TBAD$ is the normalized absolute difference between the forecasted thermal breakthrough curve and the true thermal breakthrough curve, $T_{prod,MOD}(t)$ is the thermal breakthrough model forecast corresponding to the optimal fit to tracer data, $T_{prod,TRUE}(t)$ is the true thermal breakthrough behavior (i.e. temperature at the production well over time), and t_{end} is the end time ($t_{end} = 10{,}000$ days was chosen in this case to represent a desirable reservoir lifetime).

$$TBT_{x°C} = \min\left(\boldsymbol{t}_{T_{PROD}(t) \le T_{res} - 100°C}\right) \tag{33}$$

$$TBTD_{x°C} = \left|TBT_{x°C,MOD} - TBT_{x°C,TRUE}\right| \tag{34}$$

$$PTD_{x°C} = \frac{TBTD_{x°C}}{TBT_{x°C,TRUE}} \times 100\% \tag{35}$$

where $\boldsymbol{t}_{T_{PROD}(t) \le T_{res} - 100°C}$ is the vector of all time values at which the production well temperature $T_{PROD}(t)$ is below $T_{res} - 100°C$, $TBT_{x°C}$ is the earliest time that $T_{PROD}(t)$ falls below $T_{res} - 100°C$, $TBTD_{x°C}$ is the absolute error in the model forecast $TBT_{x°C,MOD}$ of the time of the specified temperature drop with respect to the true time of the specified temperature drop $TBT_{x°C,TRUE}$, and $PTD_{x°C}$ is the percent error in the model forecast of breakthrough time (this is normalized by the true time $TBT_{x°C,TRUE}$). Note that both $TBAD$ and $PTD_{x°C}$ represent forecast error magnitudes, so the tracer types with the lowest values rank higher.

A total of 18 PSO-MADS optimizations were performed for fracture network 7 (three different starting points for each of the six tracer types), 48 PSO-MADS optimizations for fracture network 9 (6 different starting points CST, RST, and SST and 10 starting points for DRT, TNRT, and TTT), and 60 PSO-MADS optimizations for fracture network 15 (ten starting points for each of the six tracer types). Acceptable fits to the synthetic data were defined as fracture networks with objective function values less than or equal to 0.03, which corresponds to a 3% difference in the area between return curves. Acceptable fits were found for all tracer types in network 7. For network 9, acceptable fits were found for CST, RST, and SST but not for DRT, TNRT, and TTT. For network 15, acceptable fits were found for every tracer type except for TTT. Cases without acceptable fits to the synthetic data were excluded from comparison and analysis. An example of the optimal curve fit and corresponding fracture network is shown for TNRT and fracture network 15 in Figure 9.

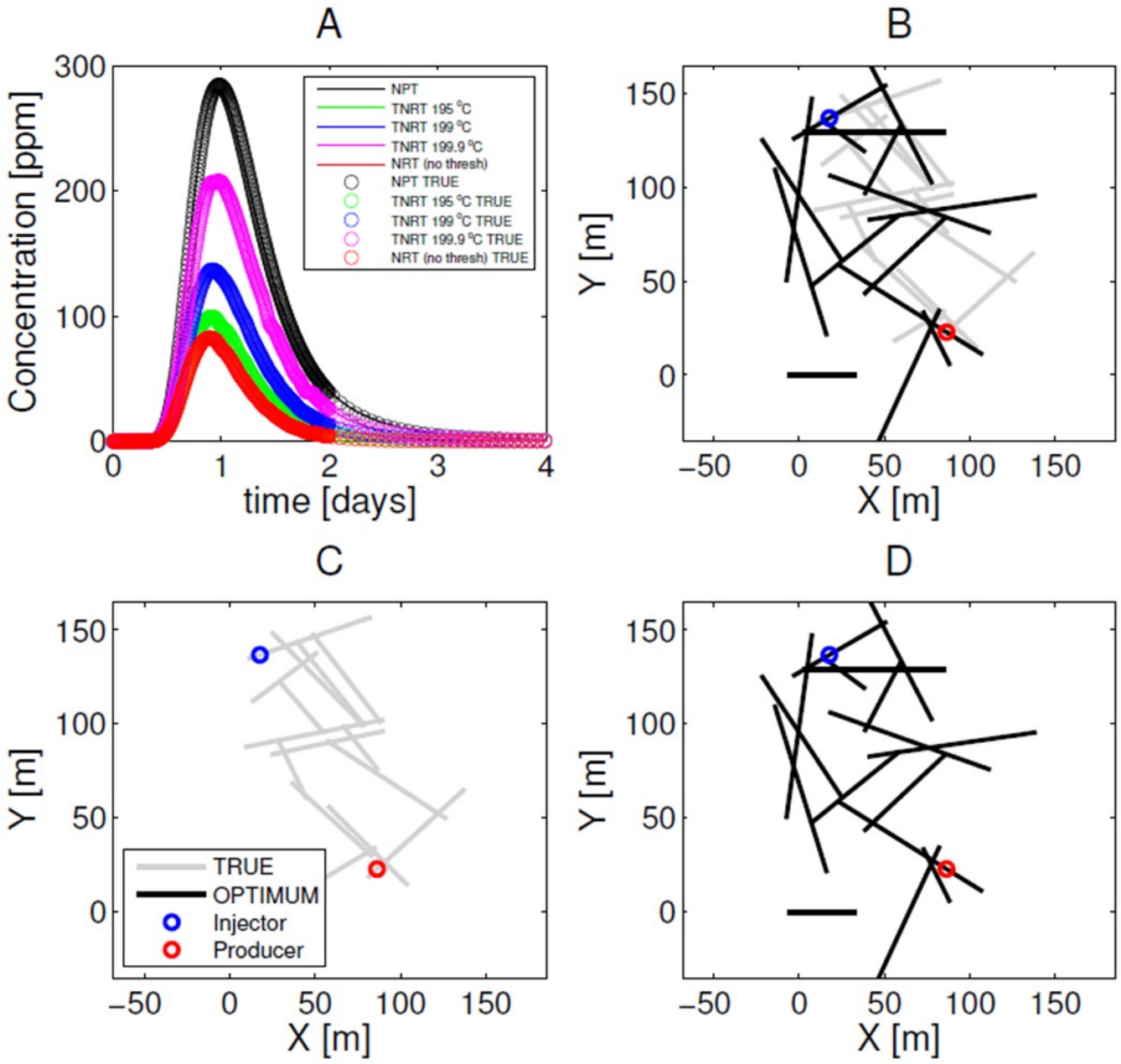

Figure 9: TNRT optimization results for fracture network 15: (A) return curve with best fit, (B) corresponding optimal fracture network with true fracture network, (C) true fracture network alone, and (D) optimal fracture network alone.

The thermal breakthrough forecasts corresponding to the optimal networks found for all tracer types are shown with the true thermal breakthrough curve for true fracture network 7 in Figure 10. The corresponding values of thermal breakthrough forecast error metrics $TBAD$ and $PTD_{x°C}$are given in Table 11. The thermal breakthrough forecasts provided by all tracer types are very accurate for fracture network 7. All had values of $TBAD < 1\%$ and values of $PTD_{x°C} < 2\%$ for all three specified temperature drops: 10°C, 20°C, and 25°C. One would not expect to ever achieve such an accurate forecast in practice, especially with CSTs. There are likely two main reasons that forecasts are so accurate. First, network 7 has very simple topology due to having only one inter-well path. Second, the thermal model used in optimizations and forecasts does not account for thermal interference between fractures, which makes the thermal response unrealistically insensitive to geometry, especially when there is only one path. As a result, the inverse problem is less unique than if thermal interference were accounted for. When thermal interference is not accounted for, a fracture network model with a single path is essentially reduced to a one-dimensional single fracture model in which the main parameter that affects temperature is the ratio of mass flowrate to heat transfer surface area. Note that fractures with different lengths also have different apertures, so fluid moves at different velocities through different fractures, so it is not quite as simple as a one-dimensional single fracture model. However, there are many different single path fracture networks with similar heat transfer surface area, so both the tracer responses and thermal behavior are fairly nonunique for network 7 when using this modeling approach. This points to the importance of using a model that can account for thermal interference in order to characterize the thermal forecast accuracy of each tracer type more accurately and definitively. Since all

thermal breakthrough forecasts are so accurate and tightly clustered, it is difficult to determine a definitive ranking of tracer types for network 7.

Table 11: Thermal breakthrough forecast error metrics $TBAD$ and $PTD_{x°C}$ for all tracer types in fracture network 7.

	CST	RST	SST	DRT	TNRT	TTT
$TBAD$	0.4%	0.29%	0.09%	0.15%	0.45%	0%
$PTD_{10°C}$	0.8%	0.8%	0.8%	0%	0.8%	0.8%
$PTD_{20°C}$	0.97%	0.97%	0.49%	0.49%	1.46%	0.97%
$PTD_{25°C}$	1.56%	0.78%	0%	0.78%	1.56%	1.17%

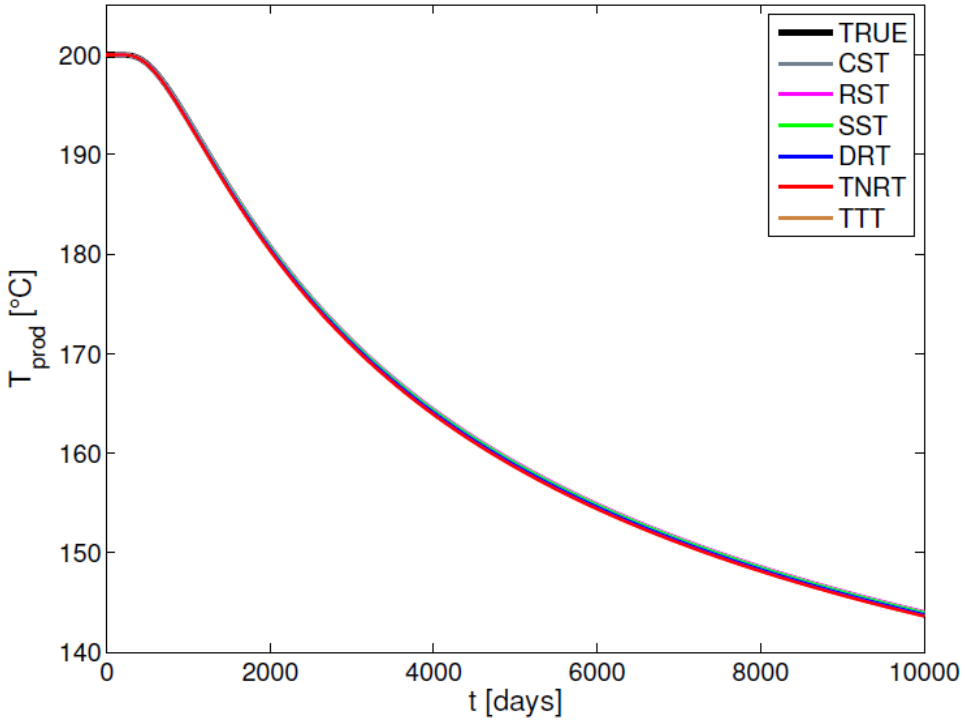

Figure 10: Thermal breakthrough curves corresponding to true fracture network and optimal fracture networks for each tracer type for true fracture fracture network 7.

The thermal breakthrough forecasts corresponding to the optimal networks found for all tracer types are shown with the true thermal breakthrough curve for true fracture network 9 in Figure 11. The corresponding values of thermal breakthrough forecast error metrics $TBAD$ and $PTD_{x°C}$ are given in Table 12 and the corresponding accuracy rankings are given in Table 13. The thermal breakthrough forecasts provided by all tracer types with acceptable fits are accurate for fracture network 9, but they are less accurate than the forecasts provided by the same tracer types in network 7. RST ranked 1st, SST ranked 2nd, and CST ranked last in all forecast accuracy metrics in network 9. $TBAD$ values range from 0.9% for RST to 3% for CST and $PTD_{x°C}$ values range from 0.4% for RST to 10.9% for CST for a 10°C temperature drop, from 2.7% for RST to 11.7% for CST for a 20°C temperature drop, and from 3.5% for RST to 12% for CST for a 25°C temperature drop. It is worth noting that the error increases for forecasts of the times of larger temperature drops because the spread between the thermal breakthrough curves increases over time (see Figure 11). The reason that the forecasts were less accurate than those for network 7 is that network 9 has four distinct inter-well paths with two flow splitting points and two flow mixing points (whereas network 7 only has one path and no mixing or splitting points). The more complex flow topology of network 9 makes tracer responses more ambiguous than if there were only a single path, because there are different possible networks with significantly different geometry that have the same tracer responses (especially for CST). Meanwhile, the thermal behavior for these networks with very similar tracer responses shows some small but noticeable deviation from that of the true network, as shown in Figure 11. The CST has the largest thermal deviation because the tracer response is not as closely related to the temperature distribution in the case of the RST or the surface area in the case of the SST. Meanwhile, there is only a small separation between the forecast accuracy of RST and that of SST, especially at late time. The metric for which RST outperformed SST the most is $PTD_{10°C}$: RST is 4% more accurate than SST with respect to this metric for network 9, which is still a relatively small difference.

Table 12: Thermal breakthrough forecast error metrics $TBAD$ and $PTD_{x°C}$ for all tracer types in fracture network 9.

	CST	RST	SST	DRT	TNRT	TTT
$TBAD$	3.0%	0.9%	1.2%	n/a	n/a	n/a
$PTD_{10°C}$	10.9%	0.4%	4.4%	n/a	n/a	n/a
$PTD_{20°C}$	11.7%	2.7%	5.0%	n/a	n/a	n/a
$PTD_{25°C}$	12.0%	3.5%	5.1%	n/a	n/a	n/a

Table 13: Tracer rankings based on thermal breakthrough forecast error metrics $TBAD$ and $PTD_{x°C}$ for all tracer types in fracture network 9.

	CST	RST	SST	DRT	TNRT	TTT
$TBAD$ rank	3	1	2	n/a	n/a	n/a
$PTD_{10°C}$ rank	3	1	2	n/a	n/a	n/a
$PTD_{20°C}$ rank	3	1	2	n/a	n/a	n/a
$PTD_{25°C}$ rank	3	1	2	n/a	n/a	n/a

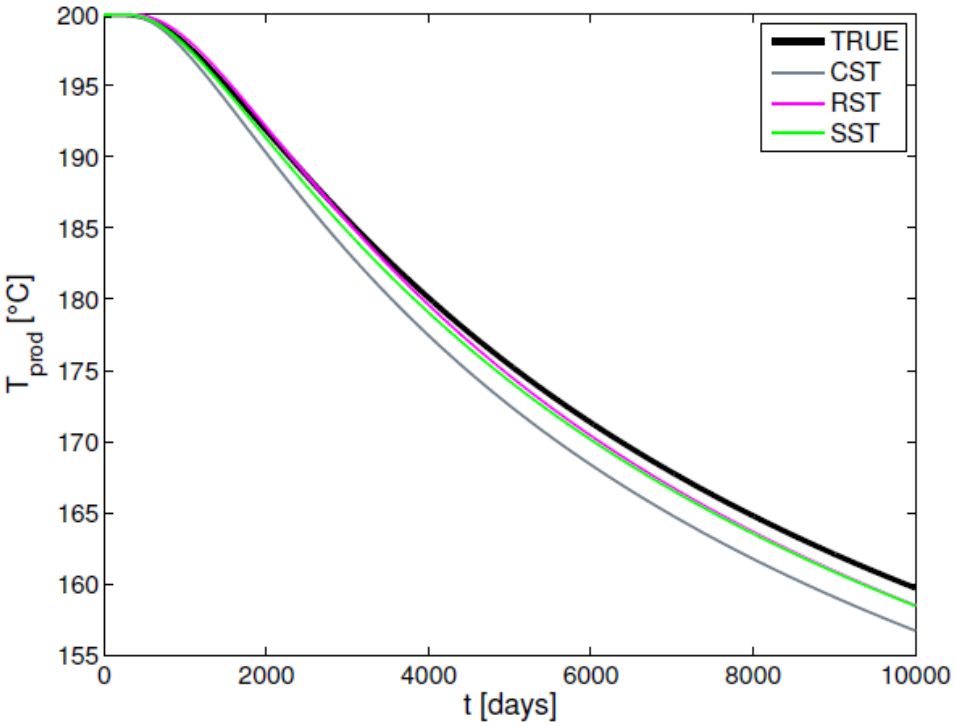

Figure 11: Thermal breakthrough curves corresponding to true fracture network and optimal fracture networks for each tracer type for true fracture fracture network 9.

The thermal breakthrough forecasts corresponding to the optimal networks found for all tracer types are shown with the true thermal breakthrough curve for true fracture network 15 in Figure 12. The corresponding values of thermal breakthrough forecast error metrics $TBAD$ and $PTD_{x°C}$ are given in Table 14 and the corresponding accuracy rankings are given in Table 15.

Table 14: Thermal breakthrough forecast error metrics $TBAD$ and $PTD_{x°C}$ for all tracer types in fracture network 15.

	CST	RST	SST	DRT	TNRT	TTT
$TBAD$	5.0%	3.3%	1.6%	1.9%	1.8%	n/a
$PTD_{10°C}$	23.4%	17.1%	8.9%	10.5%	9.4%	n/a
$PTD_{20°C}$	23.2%	15.8%	7.9%	9.3%	9.1%	n/a
$PTD_{25°C}$	22.8%	15.3%	7.8%	8.9%	9.0%	n/a

Table 15: Tracer rankings based on thermal breakthrough forecast error metrics $TBAD$ and $PTD_{x°C}$ for all tracer types in fracture network 15.

	CST	RST	SST	DRT	TNRT	TTT
$TBAD$ rank	5	4	1	3	2	n/a
$PTD_{10°C}$ rank	5	4	1	3	2	n/a
$PTD_{20°C}$ rank	5	4	1	3	2	n/a
$PTD_{25°C}$ rank	5	4	1	2	3	n/a

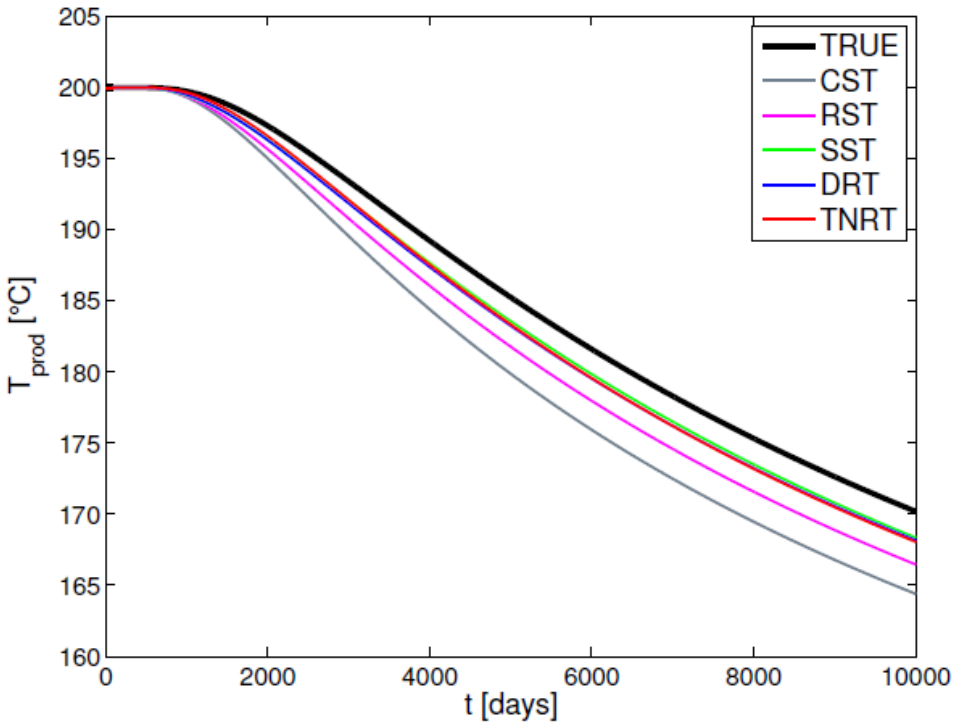

Figure 12: Thermal breakthrough curves corresponding to true fracture network and optimal fracture networks for each tracer type for true fracture fracture network 15. The thermal breakthrough curve for TTT is excluded because an acceptable match to the data was not found.

The thermal breakthrough forecasts provided by tracers in network 15 optimizations are less accurate than for either network 7 or network 9. SST ranked 1st, TNRT ranked 2nd, DRT ranked 3rd, RST ranked 4th, and CST ranked last in all forecast accuracy metrics in network 15 except for $PTD_{25°C}$, for which the rankings of DRT and TNRT were reversed and all other rankings were the same. $TBAD$ values range from 1.6% for SST to 5% for CST and $PTD_{x°C}$ values range from 8.9% for SST to 23.4% for CST for a 10°C temperature drop, from 7.9% for SST to 23.2% for CST for a 20°C temperature drop, and from 7.8% for SST to 22.8% for CST for a 25°C temperature drop. Interestingly, the error decreases slightly for forecasts of the times of larger temperature drops. One would expect the error to increase somewhat because the spread between the thermal breakthrough curves appears to increase over time, as was the case in network 9. The reason that the forecasts were less accurate than those for networks 7 and 9 is that network 15 has 16 distinct inter-well paths with many flow splitting points and mixing points (whereas network 7 only has one path and no mixing or splitting points and network 9 has four paths, two mixing points, and two splitting points). The more complex flow topology of network 15 makes tracer responses ambiguous, because there are different possible networks with significantly different geometry that have the same tracer responses (especially for CST). Meanwhile, the thermal behavior for these networks with very similar tracer responses deviates from that of the true network, as shown in Figure 12. The CST has the largest thermal deviation because the tracer response is not as closely related to the temperature distribution in the case of the DRT, TNRT, and RST or the surface area in the case of the SST.

Meanwhile, there is only a small separation between the forecast accuracy of SST, TNRT, and DRT, especially at late time. The metric for which SST significantly outperformed TNRT or DRT the most is $PTD_{10°C}$: SST is 1.6% more accurate than DRT with respect to this metric for network 15, which is still a small difference.

4. CONCLUSIONS

In this work, discrete fracture network models were developed to gain insight regarding the usefulness of the data provided by various tracer types with respect to thermal breakthrough forecasting in geothermal reservoirs. Three existing solute tracer types were modeled: conservative solute tracers (CSTs), reactive solute tracers with temperature dependent reaction kinetics (RSTs), and sorbing solute tracers that sorb reversibly to fracture walls (SSTs). Additionally three hypothetical particle tracers which have not been developed in practice were modeled: dye-releasing tracers (DRTs) that release a solute dye at a specified temperature threshold is reached, threshold nanoreactor tracers (TNRTs) with an encapsulated reaction that does not begin until a specified temperature threshold is reached, and temperature-time tracers (TTTs) capable of recording detailed temperature-time histories of each particle. An analytical model for temperature in a discrete fracture network developed by Fox (2016) was used to calculate temperature distributions used in tracer models. The tracer models were used to generate synthetic tracer data for three "true" fracture networks based on the Tamiaru fractured granite outcrop in Spain. These three fracture networks were named network 7, network 9, and network 15 and consist of of 7, 9, and 15 fractures, respectively. Both the complexity of the flow topology and the total network surface area increases with the number of fractures in these networks. These data were then fit using the PSO-MADS optimization algorithm developed by Isebor (2013) to search the space of possible fracture networks. Decision variables used in optimization were fracture location, length, and orientation and a binary "existence" variable for each fracture that turned fractures on and off in order to achieve a variable number of fractures. This resulted in a mixed-integer nonlinear programming (MINLP) problem for which PSO-MADS is well-suited. Next, the thermal model developed by Fox (2016) was utilized to calculate thermal breakthrough behavior of optimal fracture networks, and the forecast accuracy was compared for each tracer type using two forecast error metrics: $TBAD$ (the percent area between the forecasted thermal breakthrough curve and the true thermal breakthrough curve) and $PTD_{x°C}$ (the percent error in the forecast of the time of a x°C temperature drop (temperature drops of 10°C, 20°C, and 25°C were used). Finally, relationships between forecast error metrics, objective function value, and total swept surface area in the fracture network were examined.

This work resulted in the following findings:

- In network 7, all tracer types forecasted thermal breakthrough very accurately, and the accuracy metrics for different tracer types were so similar that the accuracy rankings for this network should be considered a tie. This unrealistic level of forecast accuracy was likely the result of the facts that network 7 consists of only a single inter-well fracture path and thermal interference between closely spaced fractures was not accounted for in the analytical thermal model used. This essentially reduces network 7 to a one-dimensional single fracture problem with many possible networks that match both tracer response and thermal behavior closely.

- In network 9, acceptable matches to the synthetic tracer data were found for only the three solute tracers: CST, RST, and SST. Since it would be misleading to compare the behavior of networks found in DRT, TNRT, and TTT optimizations resulting in poor matches to the data, these three tracers were excluded from rankings in network 9. RST slightly outperformed SST in all metrics, and both RST and SST outperformed CST in all metrics.

- In network 15, acceptable matches to the synthetic tracer data were found for all tracers except for TTT. Therefore, TTT excluded from rankings in network 15. Rankings for all metrics were 1) SST, 2) TNRT, 3) DRT, 4) RST, and 5) CST except for $PTD_{x°C}$, for which the DRT and TNRT rankings were reversed and all other rankings were the same. However, the difference in forecast accuracy between SST, TNRT, and DRT was small. The metric for which SST significantly outperformed TNRT or DRT the most is $PTD_{10°C}$: SST is 1.6% more accurate than DRT with respect to this metric for network 15.

- Both forecast accuracy and the relative performance of different tracer types are sensitive to the complexity of the true fracture network. Forecast accuracy for all tracers decreases as the complexity increases, and certain tracer types begin to outperform others as complexity increases (while all tracer types performed very well for the simplest case). In other words, for more complex true fracture networks, optimal fracture networks were found which fit the tracer data but had significant deviations from true thermal breakthrough behavior.

- In all cases, forecast error was very low, so clear tracer rankings were not established. This low forecast error is likely unrealistic because of both simplified two-dimensional fracture network geometry and the fact that the model did not account for thermal interference between closely spaced fractures. If this framework were used with a thermal model accounting for interference, this would likely introduce more forecast error for tracers that do not "see" temperature.

The following are promising directions for future research:

- The main limitations of this study were a result of neglecting thermal interference between closely spaced fractures, which resulted in all tracers forecasting thermal breakthrough unrealistically accurately. Therefore, it is recommended that future work be performed to evaluate the informativity of these tracers using a thermal model that can account for thermal interference, such as the parallel fracture model developed by Gringarten et al. (1975) or efficient reservoir simulation. It is hypothesized that when thermal interference is present, tracers that can "see" temperature forecast thermal breakthrough more

accurately than those that do not. This must be evaluated before it can be determined whether particle tracers provide any significant advantages over already available solute tracers.

- In order to fully understand the extent to which surface area is diagnostic regarding thermal breakthrough, sensitivity analysis should be performed in which other parameters, such as the thermal properties of fluid and rock, are varied. Accounting for thermal interference may also provide insight about the significance of surface area.

- All models in this work operate under the assumption that all fluid flow occurs in the fractures themselves, and matrix flow was neglected. It is true that flow in geothermal reservoirs is often dominated by fractures, but matrix flow is present even in low permeability rock. Therefore, it is important to repeat this assessment using a model that accounts for the effects of matrix flow on both tracer and thermal behavior. Such a study could potentially be used to determine which tracer types are most useful in each type of reservoir.

ACKNOWLEDGEMENTS

The authors would like to thank the Office of the Dean of the School of Earth, Energy & Environmental Sciences at Stanford University for supporting this work, Don Fox and Jefferson Tester at Cornell University for sharing their analytical temperature model with us, and Mohammed Alaskar, Egill Juliusson, Mohammad Karimi-Fard, Jef Caers, Mark McClure, and Obi Isebor for their time and insight.

REFERENCES

Alaskar, Mohammed, Morgan Ames, Chong Liu, Kewen Li, and Roland Horne. “Temperature Nanotracers for Fractured Reservoirs Characterization.” *Journal of Petroleum Science and Engineering* 127 (March 2015): 212–28. doi:10.1016/j.petrol.2015.01.021.

Ames, Morgan. “Temperature-Sensitive Tracers for Characterizing Fractured Geothermal Reservoirs.” Stanford University, 2016.

Ames, Morgan, and Roland N. Horne. “Modeling Temperature-Time Tracers for Projecting the Thermal Behavior of Fractured Geothermal Reservoirs.” In *Proceedings of Thirty-Ninth Workshop on Geothermal Reservoir Engineering*. Stanford, CA, 2014.

Becker, Matthew W., Paul W. Reimus, and Peter Vilks. “Transport and Attenuation of Carboxylate-Modified Latex Microspheres in Fractured Rock Laboratory and Field Tracer Tests.” *Ground Water* 37, no. 3 (May 1999): 387–95. doi:10.1111/j.1745-6584.1999.tb01116.x.

Dean, Cynthia, Paul Reimus, and Dennis Newell. “Evaluation of a Cation Exchanging Tracer to Interrogate Fracture Surface Area in EGS Systems.” In *Proceedings of Thirty-Seventh Workshop on Geothermal Reservoir Engineering*. Stanford, CA, 2012.

Dean, Cynthia, Paul Reimus, Jeffrey Oates, Peter Rose, Dennis Newell, and Susan Petty. “Laboratory Experiments to Characterize Cation-Exchanging Tracer Behavior for Fracture Surface Area Estimation at Newberry Crater, OR.” *Geothermics* 53 (January 2015): 213–24. doi:10.1016/j.geothermics.2014.05.011.

den Iseger, Peter. “Numerical Transform Inversion Using Gaussian Quadrature.” *Probability in the Engineering and Informational Sciences* 20, no. 01 (2006): 1–44. doi:10.1017/S0269964806060013.

Fox, Don Bruce. “Thermal Hydraulic Modeling of Discretely Fractured Geothermal Reservoirs.” Cornell University, 2016.

Gringarten, A. C., P. A. Witherspoon, and Yuzo Ohnishi. “Theory of Heat Extraction from Fractured Hot Dry Rock.” *Journal of Geophysical Research* 80, no. 8 (March 10, 1975): 1120–24. doi:10.1029/JB080i008p01120.

Hawkins, Adam, Don Fox, Russell Zhao, Jefferson Tester, Lawrence Cathles, Donald Koch, and Matthew Becker. “Predicting Thermal Breakthrough from Tracer Tests: Simulations and Observations in a Low-Temperature Field Laboratory.” In *Proceedings of Fortieth Workshop on Geothermal Reservoir Engineering*. Stanford, CA, 2015.

Horne, R. N. “Reservoir Engineering of Reinjection.” presented at the Geothermal Training Program, UN University, Reykjavik, Iceland, 2010.

Humphrey, Andrew R., Amr Abdel-Fattah, and Paul Reimus. “Software Management Report for ReLap Version 2.0.” Los Alamos National Laboratory, 2001.

Isebor, Obiajulu J., Louis J. Durlofsky, and David Echeverría Ciaurri. “A Derivative-Free Methodology with Local and Global Search for the Constrained Joint Optimization of Well Locations and Controls.” *Computational Geosciences* 18, no. 3–4 (August 2014): 463–82. doi:10.1007/s10596-013-9383-x.

Isebor, Obiajulu J., David Echeverría Ciaurri, and Louis J. Durlofsky. “Generalized Field-Development Optimization With Derivative-Free Procedures.” *SPE Journal* 19, no. 05 (October 1, 2014): 891–908. doi:10.2118/163631-PA.

Isebor, Obiajulu Joseph. “Derivative-Free Optimization for Generalized Oil Field Development.” Stanford University, 2013.

James, Scott C, and Constantinos V Chrysikopoulos. “An Efficient Particle Tracking Equation with Specified Spatial Step for the Solution of the Diffusion Equation.” *Chemical Engineering Science* 56, no. 23 (December 2001): 6535–43. doi:10.1016/S0009-2509(01)00344-X.

Juliusson, E. “Characterization of Fractured Geothermal Reservoirs Based on Production Data.” Stanford University, 2012.

Juliusson, E. *DenIseger*, 2010.

Kuhn, H. “The Hungarian Method for the Assignment Problem.” *Naval Research Logistic Quarterly* 2 (1955): 83–97.

Leecaster, Kevin, Bridget Ayling, Greg Moffitt, and Pete Rose. “Use of Safranin T as a Reactive Tracer for Geothermal Reservoir Characterization.” In *Proceedings of Thirty-Seventh Workshop on Geothermal Reservoir Engineering*. Stanford, CA, 2012.

Likhachev, E. R. “Dependence of Water Viscosity on Temperature and Pressure.” *Technical Physics* 48, no. 4 (April 2003): 514–15. doi:10.1134/1.1568496.

Maloszewski, P., and A. Zuber. “Interpretation of Artificial and Environmental Tracers in Fissured Rocks with a Porous Matrix.” In *Isotope Hydrology 1983*, 635–51. Vienna: International Atomic Energy Agency, 1983. http://www.iaea.org/inis/collection/NCLCollectionStore/_Public/38/052/38052798.pdf#page=649.

Munkres, James. “Algorithms for the Assignment and Transportation Problems.” *Journal of the Society for Industrial and Applied Mathematics* 5 (1957): 32–38.

Olson, Jon E. “Sublinear Scaling of Fracture Aperture versus Length: An Exception or the Rule?” *Journal of Geophysical Research* 108, no. B9 (2003). doi:10.1029/2001JB000419.

Place, Joachim, Edouard Le Garzic, Yves Geraud, Marc Diraison, and Judith Sausse. “Characterisation of the Structural Control on Fluid Flow Paths in Fractured Granites.” In *Proceedings of Thirty-Sixth Workshop on Geothermal Reservoir Engineering*. Stanford, CA, 2011.

Plummer, Mitchell A., Carl D. Palmer, Laurence C. Hull, and Earl D. Mattson. “Sensitivity of a Reactive-Tracer Based Estimate of Thermal Breakthrough In an EGS to Properties of the Reservoir and Tracer.” In *Proceedings of Thirty-Seventh Workshop on Geothermal Reservoir Engineering*. Stanford, CA, 2012.

Redden, George, Mark Stone, Karen E. Wright, Earl Mattson, Carl D. Palmer, Harry Rollins, Mason Harrup, and Laurence C. Hull. “Tracers For Characterizing Enhanced Geothermal Systems.” In *Proceedings of Thirty-Fifth Workshop on Geothermal Reservoir Engineering*. Stanford, CA, 2010.

Reimus, Paul W., Timothy J. Callahan, S. Doug Ware, Marc J. Haga, and Dale A. Counce. “Matrix Diffusion Coefficients in Volcanic Rocks at the Nevada Test Site: Influence of Matrix Porosity, Matrix Permeability, and Fracture Coating Minerals.” *Journal of Contaminant Hydrology* 93, no. 1–4 (August 15, 2007): 85–95. doi:10.1016/j.jconhyd.2007.01.017.

Reimus, Paul W, Marc J Haga, Andrew I Adams, Timothy J Callahan, H.J Turin, and Dale A Counce. “Testing and Parameterizing a Conceptual Solute Transport Model in Saturated Fractured Tuff Using Sorbing and Nonsorbing Tracers in Cross-Hole Tracer Tests.” *Journal of Contaminant Hydrology* 62–63 (April 2003): 613–36. doi:10.1016/S0169-7722(02)00185-7.

Reimus, Paul, Mark Williams, Vince Vermeul, Peter Rose, Kevin Leecaster, Bridget Ayling, Raphael Sanjuan, Morgan Ames, Cynthia Dean, and Dick Benoit. “Use of Tracers To Interrogate Fracture Surface Area In Single-Well Tracer Tests In EGS Systems.” In *Proceedings of Thirty-Seventh Workshop on Geothermal Reservoir Engineering*. Stanford, CA, 2012.

Reimus, P. W. “The Use of Synthetic Colloids in Tracer Transport Experiments in Saturated Rock Fractures.” University of New Mexico, 1995.

Riesen, Kaspar, and Horst Bunke. “Approximate Graph Edit Distance Computation by Means of Bipartite Graph Matching.” *Image and Vision Computing* 27, no. 7 (June 2009): 950–59. doi:10.1016/j.imavis.2008.04.004.

Rose, Peter E., and Michael C. Adams. “The Application of Rhodamine WT As a Geothermal Tracer.” In *Transactions - Geothermal Resources Council*, 18:237–40. Davis, CA, 1994.

Tester, J. W., B. A. Robinson, and J. H. Ferguson. “Inert and Reacting Tracers for Reservoir Sizing in Fractured, Hot Dry Rock Systems.” In *Proceedings of Eleventh Workshop on Geothermal Reservoir Engineering*. Stanford, CA, 1986.

Williams, M. D., P. W. Reimus, V. R. Vermeul, P. E. Rose, C. A. Dean, T. B. Watson, D. L. Newell, K. B. Leecaster, and E. M. Brauser. “Development of Models to Simulate Tracer Tests for Characterization of Enhanced Geothermal Systems.” Pacific Northwest National Laboratory, 2013. http://www.pnnl.gov/main/publications/external/technical_reports/PNNL-22486.pdf.

Williams, M. D., V. R. Vermeul, P. W. Reimus, D. L. Newell, and T. B. Watson. “Development of Models to Simulate Tracer Behavior in Enhanced Geothermal Systems - Status Report.” Pacific Northwest National Laboratory, 2010. http://www.pnl.gov/main/publications/external/technical_reports/PNNL-19523.pdf.

Zhou, Quanlin, Hui-Hai Liu, Fred J. Molz, Yingqi Zhang, and Gudmundur S. Bodvarsson. “Field-Scale Effective Matrix Diffusion Coefficient for Fractured Rock: Results from Literature Survey.” *Journal of Contaminant Hydrology* 93, no. 1–4 (August 2007): 161–87. doi:10.1016/j.jconhyd.2007.02.002.